Electronic Supplementary Material

High-performance silicon nanocomposite based ionic actuators

Chao Lu[a], Quanzhang Huang[b] and Xi Chen[a*]

[a] Department of Earth and Environmental Engineering, Columbia University, New York, NY 10027, USA.

[b] School of Chemical Engineering, Northwest University, Xi'an, Shaanxi, 710069, China.

* Corresponding author. Email: xichen@columbia.edu

Experimental section

Synthesis of silicon@graphene nanomaterials: Firstly, 10 mg silicon nanomaterials was dispersed with 1 mg poly(diallyldimethylammonium chloride) (PDDA) in 20 mL dimethylformamide (DMF) under stirring for 12 h. The excess PDDA was removed by centrifugation and washing for 3 times. Afterwards, 3.5 mg graphene oxide was mixed with silicon/PDDA material in solution by ultrasonication treatment for 2 h and then let it stand still for 24 h. Subsequently, the solution was filtered and rinsed with deionized water and ethonal for 3 times. Then, the dispersion were treated with vacuum drying at 150 ^{o}C for 24 h. Next, the obtained powder was treated with HI acid reduction process. Finally, silicon@graphene nanomaterials were obtained after calcining at 500 ^{o}C for 3 h in tube furnace under argon atmosphere.

Fabrication of polyelectrolyte layer: Firstly, 4.24 g lithium chloride (LiCl) was dissolved in 100 mL deionized water to form 1 M LiCl solution. Then, Nafion film was immersed into LiCl solution at 60 ^{o}C for 36 h. Finally, the single-ion polyelectrolyte layer was obtained after rinsing by deionized water 3 times and then drying at 50 ^{o}C for 24 h.

Preparation of electrode layer and actuators: Firstly, 95 mg silicon@graphene nanomaterials and 5 mg PVdF were disperse in 5 mL methylpyrrolidone (NMP) under

ultrasonication for 2 h. Subsequently, the dispersion was casted onto the mould and then peeled off as a freestanding electrode layer after drying at 70 °C for 9 h. Lastly, the actuator was assembled by laminating two pieces of electrode films with polyelectrolyte separator through hot pressing method. Actuators with different massloadings were prepared by same process with different concentration of electrode material dispersion. Thickness of the actuator is measured as 926 μm.

Characterization techniques: SEM and TEM characterizations were made with SIGMA VP and FEI TALOS F200X instruments, respectively. Raman spectra were tested by Horiba XploRA. X-ray powder diffraction spectra was measured by Antron-Paar TTK 450. Nitrogen adsorption experiments was conducted using Micromeritics ASAP 2020 HV BET analyzer. Electrochemical and electromechanical characterizations were made with Bio-logic Potentiostat VMP3.

Single-ion conductors are seldom reported as polyelectrolytes for ionic actuators. The most commonly used polyelectrolytes in ionic actuators are ionogels, which are composed of polymer substrates and ionic liquids, such as PVDF/$EMIBF_4$,[1] TPU/$EMIBF_4$,[2] SPBI/$EMIBF_4$,[3] PEO-NBR/$EMIBF_4$,[4] and PS-b-PSS/$EMIBF_4$.[5] The ionogels provide wide potential window, air-working stability and non-flammability, which are important to improve actuation properties and cyclic stability of ionic actuators. But this complicated ionic environments definitely cause inhomogeneous diffusion of cations and anions during charge-discharge processes and result in inferior performances. Single-ion conductor used in this study avoids the issues of ionogels mentioned above, because there exists only one mobile ion in polyelectrolyte without any aqueous organic or inorganic solvents. As the anions are fixed on polymer frameworks with cations aside keeping electroneutrality, ions will not let out as conventional ionogels or hydrogels, which will improve safety for practical applications in future.

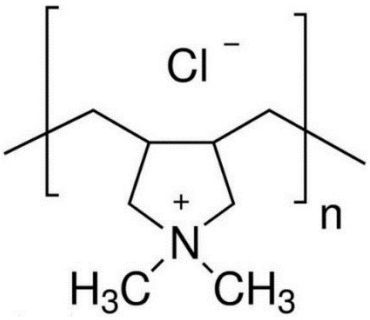

Fig. S1 Chemical structure of poly (dimethyldiallylammonium chloride).

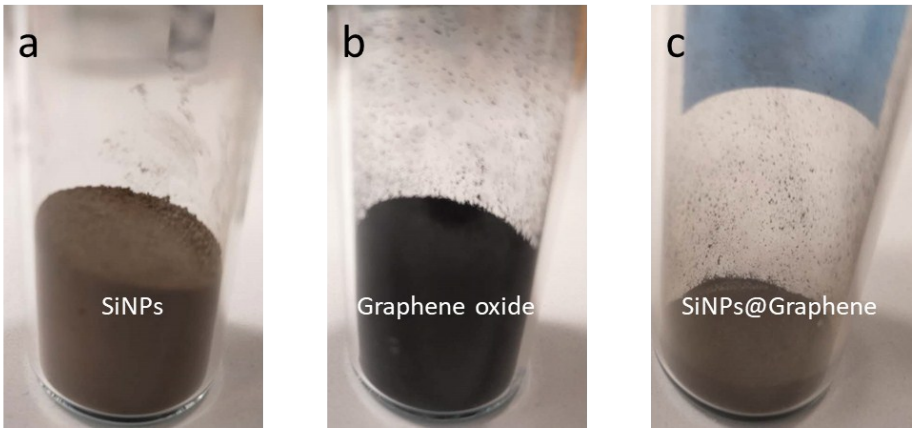

Fig. S2 Optical images of a SiNPs, b graphene oxide and c Si@Graphene, respectively.

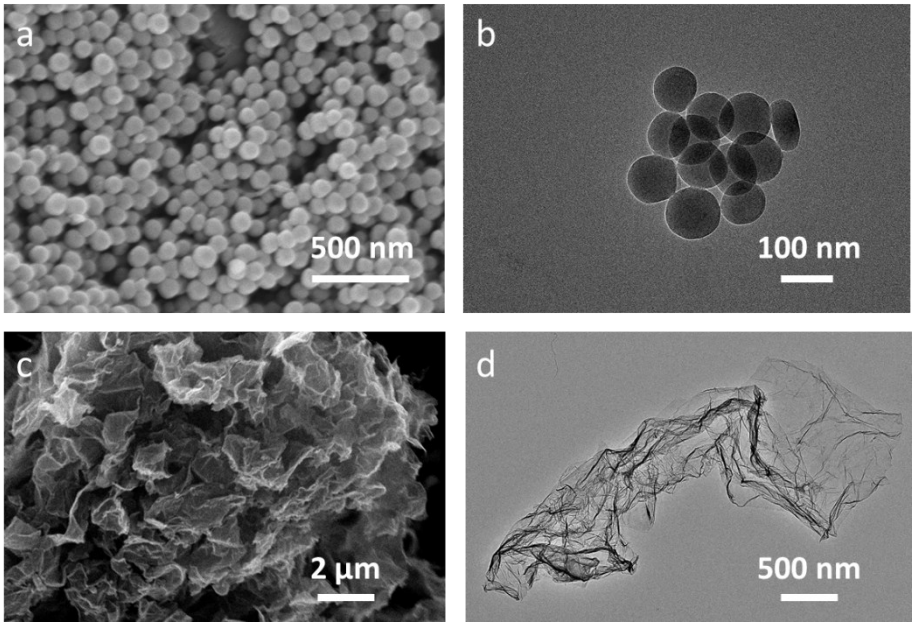

Fig. S3 (a and c) SEM images of SiNPs and graphene oxide. (b and d) TEM images of SiNPs and graphene oxide.

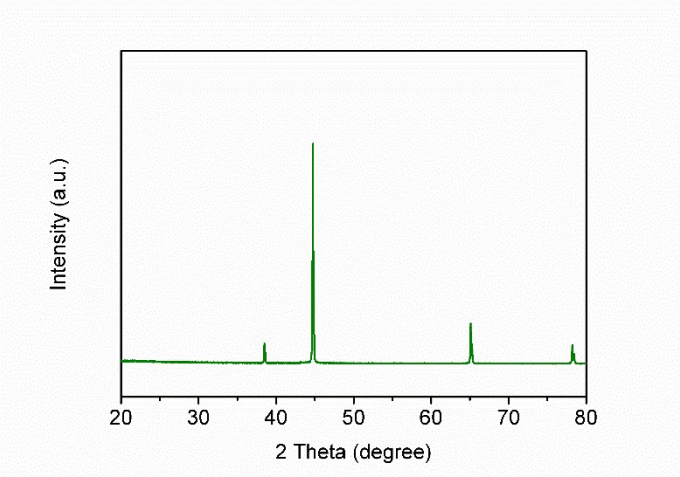

Fig. S4 XRD pattern of sample stage.

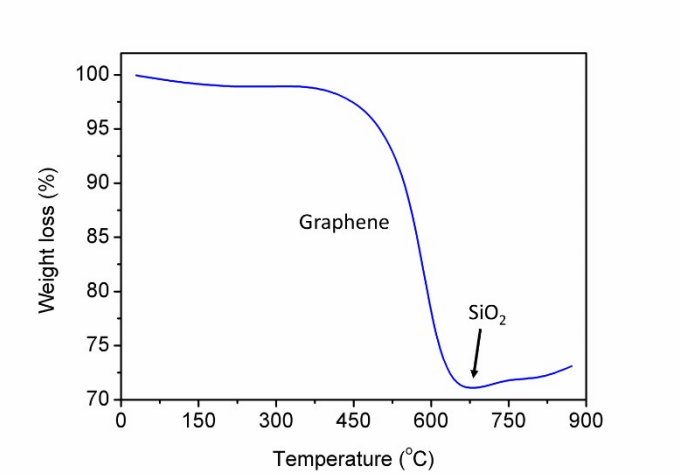

Fig. S5 TGA trace of Si@graphene materials recorded in air at rate of 5 ^{o}C min^{-1}.

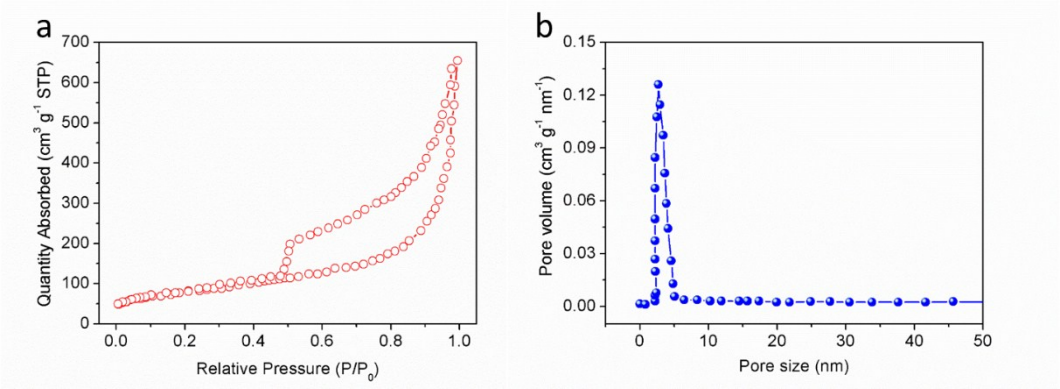

Fig. S6 a Nitrogen sorption isotherms of graphene. b Pore size distribution of graphene.

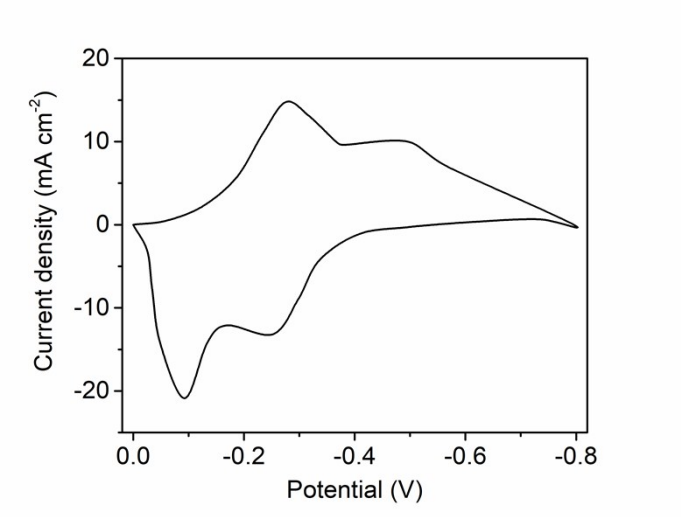

Fig. S7 Cyclic voltammetry result of the electrode material in three-electrode system with scan rate of 0.5 V s^{-1} under potential range from 0 to -0.8 V.

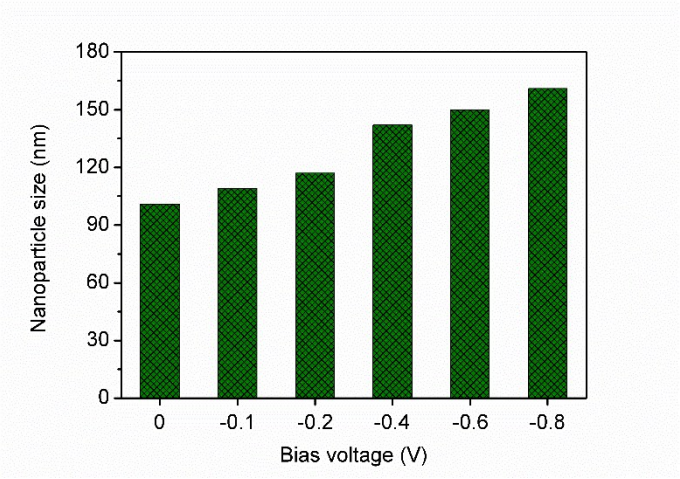

Fig. S8 Silicon particle size variation of Si@Graphene electrode under different bias voltages through ex-situ cryogenic TEM characterization.

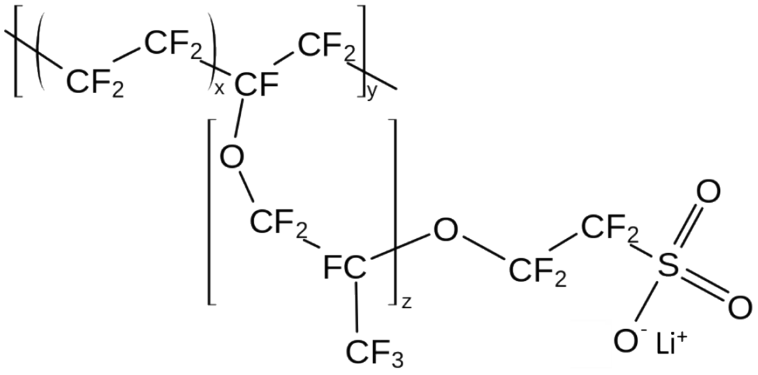

Fig. S9 Chemical structure of Nafion-Li solid polymer electrolyte.

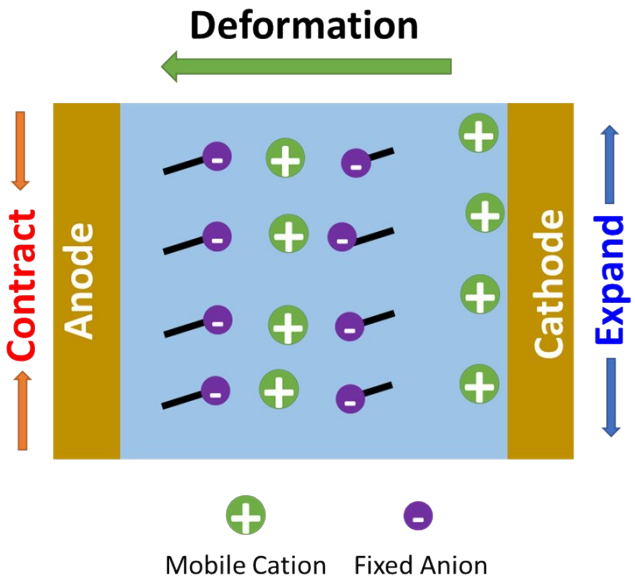

Fig. S10 Actuation mechanism of actuators assembled with single-ion conductor.

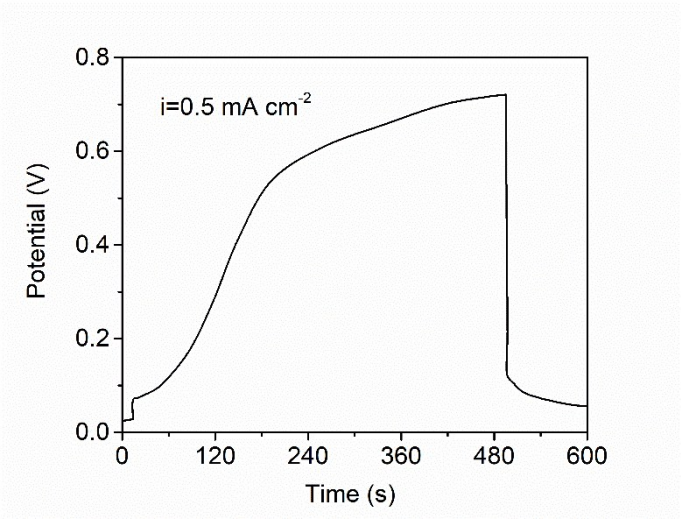

Fig. S11 Chronopotentiometry curve of the actuator at current density of 0.5 mA cm^{-2}.

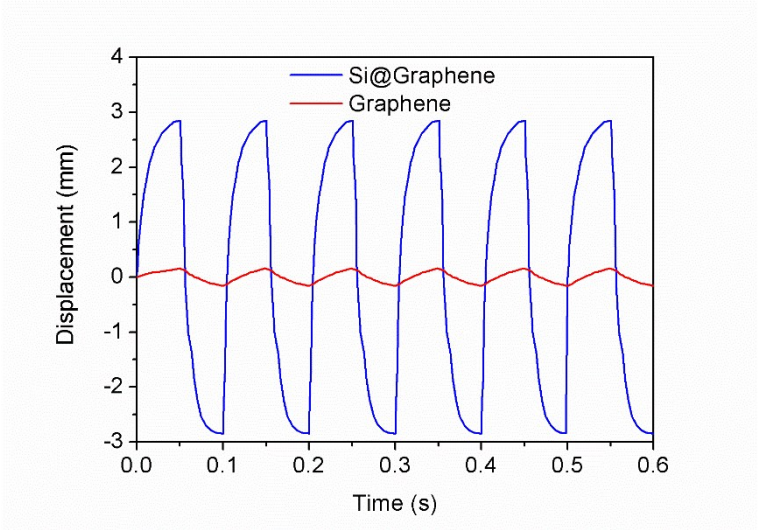

Fig. S12 Displacements of actuators based on Si@Graphene and graphene electrodes at the frequency of 10 Hz under 0.8 V.

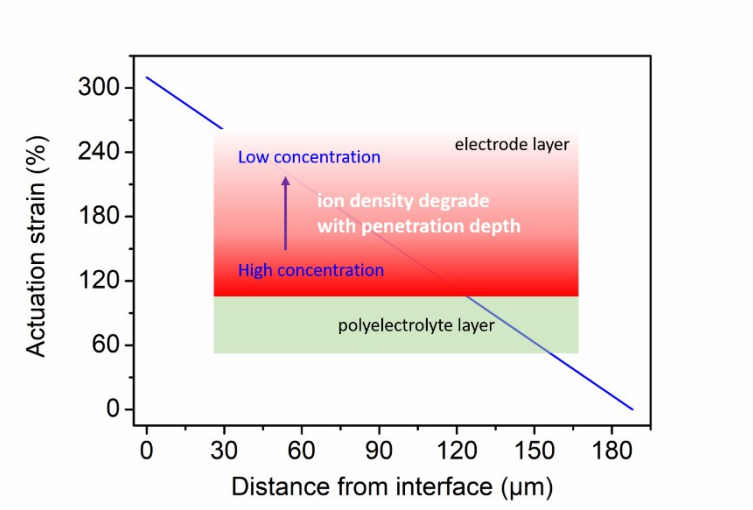

Fig. S13 Linear relationship assumption of actuation strain of SiNPs as function of distance from interface in electrode layer. Inset shows scheme of ion density distribution in electrode layer.

Table S1 Comparison of actuation performances of various materials based ionic actuators.

Electrode materials	Displacement (mm)	Blocking force (mN)	Energy density (kJ m^{-3})	References
Si@Graphene	15	71	10.91	This study
PEDOT	3.8	0.15	0.07	Sens. Actuators, B, 2014, 194, 59
Graphene	12	0.6	0.07	Materials 2020, 13, 656
CNTs	8	1.38	0.14	Sens. Actuators, A, 2007, 133, 117
Graphene/CNTs	4	1.92	0.21	Adv. Mater. 2012, 24, 4317
Au	13.1	5.42	0.03	Electrochim. Acta, 2014, 129, 450
g-C_3N_4	6.09	0.93	1.73	Nat. Commun. 2015, 6, 7258
PEDOT/CNT	15.7	1.43	1.68	RSC Adv. 2017, 7, 31264
MXene	2	4.71	6.2	Science Robotics, 2019, 4, eaaw7797
Graphdiyne	16	3.37	11.5	Nat. Commun.

				2018, 9, 752
Black phosphorus	21.4	2.65	6	Adv. Mater. 2019, 31, 1806492

Supplementary Notes

The neutral-layer-strain coefficient C_{ε_0}

$$C_{\varepsilon_0} = E_1 t_1 / 2E_1 t_1 + E_2 t_2 \tag{S1}$$

The curvature-radius coefficient C_ρ

$$C_\rho = \frac{2}{(t_2 + t_1)} \left\{ \frac{E_2 t_2^3}{12 E_1 t_1} + \frac{2}{3} [t_1^2 + \frac{3 t_1 t_2}{2} + \frac{3 t_2^2}{4}] \right\} \tag{S2}$$

Geometric deformation relationships for Fig.3

$$\begin{aligned} L &= L_0(1+\varepsilon_0) = \rho\theta \\ \theta &= \cos^{-1}(\frac{\rho - w}{\rho}) \end{aligned} \tag{S3}$$

Eshelby eigen strain ε^* can be obtained as following

$$\varepsilon^* = -\boldsymbol{D}\varepsilon_0 + \boldsymbol{F}\varepsilon^\theta \tag{S4}$$

where

$$\begin{aligned} \boldsymbol{D} &= [(\boldsymbol{C}_1 - \boldsymbol{C}_0)\boldsymbol{E} + \boldsymbol{C}_0]^{-1}(\boldsymbol{C}_1 - \boldsymbol{C}_0) \\ \boldsymbol{F} &= [(\boldsymbol{C}_1 - \boldsymbol{C}_0)\boldsymbol{E} + \boldsymbol{C}_0]^{-1}\boldsymbol{C}_1 \end{aligned}$$

The stress tensor of the inclusion

$$\langle \sigma \rangle_w = \sigma_0 - \boldsymbol{A}\varepsilon_0 + \boldsymbol{B}\varepsilon_\theta \tag{S5}$$

where

$$\begin{aligned} \boldsymbol{A} &= \boldsymbol{C}_0 \boldsymbol{E} - \boldsymbol{I} \left[\boldsymbol{E} + (\boldsymbol{C}_1 - \boldsymbol{C}_0)^{-1} \boldsymbol{C}_0 \right]^{-1} \\ \boldsymbol{B} &= \left\{ [\boldsymbol{C}_0 (\boldsymbol{I} - \boldsymbol{E}^{-1})]^{-1} - \boldsymbol{C}_1^{-1} \right\}^{-1} \end{aligned}$$

The average strain $\boldsymbol{\varepsilon}_0$ graphene matrix can be written as

$$\boldsymbol{\varepsilon}_0 = f\boldsymbol{M}\boldsymbol{\varepsilon}^\theta \tag{S6}$$

where $\boldsymbol{M} = -(\boldsymbol{C}_0 - f\boldsymbol{A})^{-1}\boldsymbol{B}$.

$\boldsymbol{N}$ is an isotropic fourth-order tensor with two independent parameters, and it can

be abbreviated as N_1, N_2 ,

$$\boldsymbol{N}=f[\boldsymbol{M}-f\boldsymbol{EDM}+\boldsymbol{EF}] \tag{S7}$$

$$N_{ijkl}=\frac{1}{3}N_1\delta_{ij}\delta_{kl}+\frac{1}{2}N_2(\delta_{il}\delta_{jk}+\delta_{ik}\delta_{jl}-\frac{2}{3}\delta_{ij}\delta_{kl}) \tag{S8}$$

N_1 and N_2 has the following form

$$\begin{aligned} N_{11}&=f(R+\alpha F_1)\\ N_2&=f(R_2+\beta F_2) \end{aligned} \tag{S9}$$

$$\alpha=\frac{3K_0}{3K_0+4G_0},\quad \beta=\frac{6(K_0+2G_0)}{5(3K_0+4G_0)} \tag{S10}$$

$$\begin{aligned} R_1&=\frac{K_1(1-\alpha)}{(K_1-K_0)(1-f)\alpha+(1-f)K_0+fK_1}\frac{(K_1-K_0)(1-f)\alpha+K_0}{(K_1-K_0)\alpha+K_0}\\ R_2&=\frac{G_1(1-\beta)}{(G_1-G_0)(1-f)\beta+(1-f)G_0+fG_1}\frac{(G_1-G_0)(1-f)\beta+G_0}{(G_1-G_0)\beta+G_0} \end{aligned} \tag{S11}$$

$$F_1=\frac{K_1}{(K_1-K_0)\alpha+K_0},\quad F_2=\frac{G_1}{(G_1-G_0)\beta+G_0} \tag{S12}$$

where the K_0 and K_1 denote bulk modulus of matrix and inclusion, G_0 and G_1 the shear modulus of matrix and inclusion respectively.

the principal strain component $\bar{\varepsilon}_{11}$

$$\begin{aligned} \bar{\varepsilon}_{11}&=[\boldsymbol{N}_{1111}\varepsilon_{11}^{\theta}+\boldsymbol{N}_{1122}\varepsilon_{22}^{\theta}+\boldsymbol{N}_{1133}\varepsilon_{33}^{\theta}]\\ &=[\boldsymbol{N}_{1111}+\boldsymbol{N}_{1122}+\boldsymbol{N}_{1133}]\varepsilon_{11}^{\theta}\\ &=n\varepsilon_{11}^{\theta} \end{aligned} \tag{S13}$$

According to previous reported works using in-operando neutron reflectometry[6], Li ion coefficient (x) in Li_xSi compound presents linear relationship with volume expansion of the compound ($V/V_0=0.825x+0.9275$). In this study, volume expansion (V/V_0) of SiNPs achieves at 410%, thus Li ion coefficient (x) is calculated as 3.845 with the formula, which is also in accord with other related works[7, 8]. Density functional theory was applied to evaluated the relationship[9] between Li ion coefficient and modulus of Li_xSi compound as follow $E_{LixSi}=(18.90x+90.13)/(1+x)$. Modulus of Li_xSi compound in this work was calculated as 33.74 Gpa based on the fitting formula above,

taking the other parameters ν_1=0.218, $E_0 = 32\text{GPa}$, $\nu_0 = 0.17$, resultingly the parameter *n* equals to 0.1924.

References

1. C. Lu, Y. Yang, J. Wang, R. Fu, X. Zhao, L. Zhao, Y. Ming, Y. Hu, H. Lin, X. Tao, Y. Li and W. Chen, *Nat. Commun.*, 2018, **9**, 752.
2. D. Wang, C. Lu, J. Zhao, S. Han, M. Wu and W. Chen, *RSC Adv.*, 2017, **7**, 31264-31271.
3. M. Kotal, J. Kim, K. J. Kim and I. K. Oh, *Adv. Mater.*, 2016, **28**, 1610-1615.
4. G. Wu, Y. Hu, Y. Liu, J. Zhao, X. Chen, V. Whoehling, C. Plesse, G. T. Nguyen, F. Vidal and W. Chen, *Nat. Commun.*, 2015, **6**, 7258-7265.
5. V. H. Nguyen, J. Kim, R. Tabassian, M. Kotal, K. Jun, J. H. Oh, J. M. Son, M. T. Manzoor, K. J. Kim and I. K. Oh, *Advanced Science*, 2019, **6**, 1801196.
6. K. Jung, J. Nam and H. Choi, *Sens. Actuators, A*, 2003, **107**, 183-192.
7. V. Palmre, E. Lust, A. Jänes, M. Koel, A.-L. Peikolainen, J. Torop, U. Johanson and A. Aabloo, *J. Mater. Chem.*, 2011, **21**, 2577-2583.
8. V. Chevrier and J. R. Dahn, *J. Electrochem. Soc.*, 2009, **156**, A454-A458.
9. C. Lu and X. Chen, *J. Power Sources*, 2020, **448**, 227587.